

Article

Numerical Study of a Miniaturized, 1–3 Piezoelectric Composite Focused Ultrasound Transducer

Howuk Kim ^{1,*}  and Xiaoning Jiang ²

¹ Department of Mechanical Engineering, Inha University, 100, Inha-ro, Michuhol-gu, Incheon 22212, Republic of Korea

² Department of Mechanical and Aerospace Engineering, North Carolina State University, Engineering Bldg 3, Raleigh, NC 27695, USA

* Correspondence: howuk@inha.ac.kr; Tel.: +82-32-860-7317

Featured Application: Interstitial focused ultrasound, optimal transducer design.

Abstract: This study aimed to develop an optimal methodology for the design of a miniaturized, 1–3 piezoelectric composite focused ultrasound transducer. Miniaturized focused ultrasound (FUS) devices, generally guided through catheters, have received considerable attention in the biomedical and ultrasound fields as they can overcome the technical restrictions of typical FUS transducers. However, miniaturized transducers cannot readily generate a high acoustic intensity because of their small aperture sizes and the vibration mode coupling. As such, 1–3 composite transducers, having a high electromechanical coupling and efficient vibration directivity, break through the current technical restrictions. However, the systematic methodology for designing miniaturized FUS transducers has not been thoroughly discussed so far. Therefore, in this study, we designed 1–3 piezoelectric composite transducers using analytical and numerical methods. Specifically, extensive parametric studies were performed through finite element analysis under the coupled field with piezoelectricity, structural vibration, and acoustic pressure. The simulation results confirmed that the optimal design of the 1–3 composite type transducer produces much higher (>160%) acoustic pressure output at the focal point than the single-phase device. Furthermore, the array type of the interstitial transducer was predicted to produce an unprecedented acoustic intensity of approximately 188 W/cm² under a short duty cycle (1%). This study will provide valuable technical methodology for the development of interstitial, 1–3 composite FUS transducers and the selection of optimal design parameters.

Keywords: 1–3 composite; piezoelectric; focused ultrasound; miniaturized transducer; transducer design



Citation: Kim, H.; Jiang, X. Numerical Study of a Miniaturized, 1–3 Piezoelectric Composite Focused Ultrasound Transducer. *Appl. Sci.* **2023**, *13*, 615. <https://doi.org/10.3390/app13010615>

Academic Editor: Giuseppe Lacidogna

Received: 14 December 2022

Revised: 29 December 2022

Accepted: 30 December 2022

Published: 2 January 2023



Copyright: © 2023 by the authors. Licensee MDPI, Basel, Switzerland. This article is an open access article distributed under the terms and conditions of the Creative Commons Attribution (CC BY) license (<https://creativecommons.org/licenses/by/4.0/>).

1. Introduction

Ultrasound has been commonly used for medical purposes owing to its safety, effective penetration, and radiation-free characteristics [1,2]. Focused ultrasound (FUS) is one of the emerging technologies in the biomedical field. FUS concentrates acoustic energy to the focal spot, thereby heating or ablating the target issue [3]. FUS waves targeted at a tissue cause a vibration of the biomolecules, which results in the generation of frictional heat [4]. The rise in temperature of a tissue beyond a certain threshold causes the coagulative necrosis of the tissue [5].

Conventional high-intensity FUS performs non-intrusively, delivering ultrasound waves from the outer side of the body [6,7]. The conventional modality is still attractive as a noninvasive medical treatment. However, non-intrusive FUS techniques should be performed with care, as FUS delivered in an indirect manner may cause unwanted damage to healthy tissue and complications after the treatment [8]. Moreover, some bio-organs that lie behind a media with a high acoustic impedance, such as bones, are challenging

to treat with the noninvasive FUS method [9]. Therefore, precise monitoring of the target lesion, such as with MRI or CT imaging, may be required during noninvasive FUS ultrasound treatment [9,10].

In recent years, interstitial FUS has been actively studied to overcome the technical restrictions in the noninvasive FUS [11–13]. Miniaturized FUS transducers, generally directed through catheters, are capable of heating and directly ablating the target tissue by transmitting acoustic waves near the target [14–16]. The direct application of acoustic waves can minimize the potential of damage in unwanted tissues compared to the typical noninvasive FUS modality. However, the geometric restriction of the aperture of the device is one of its most challenging issues as the aperture size directly affects the efficiency of the acoustic transmission.

Piezoelectric materials, such as PZT, are most commonly used as active layers of FUS devices owing to their effective energy conversion and the fast response time [17]. PZT materials, due to the benefits, have been commonly used in various engineering fields, including sound and vibration control, biomedical imaging, structural health monitoring, and so on [18–21]. The thickness and the piezoelectric property of the active layer determine the operating frequency of the device when the vibration modes along the thickness and the lateral directions are decoupled [22]. However, as for interstitial, miniaturized, FUS transducers, in the case where the lateral dimension becomes similar to the thickness, the vibration mode along the thickness direction is coupled with the lateral mode, resulting in an inefficient transmission of acoustic waves.

The composite type of the active element may not have the geometric restrictions of the single-phase piezoelectric transducers. For example, a 1–3 composite (1-D connection of the piezoelectric element and a 3-D connection of polymer matrix) piezoelectric material comprises small-width piezoelectric columns combined with a passive media such as epoxy [23]. All the individual active elements have a relatively small width compared to the thickness of the device; thus, it exhibits a distinguished thickness vibration mode [11,23]. In addition, the 1–3 composite structure normally decreases the overall acoustic impedance level, reducing the acoustic mismatch between the transducer and the target acoustic medium such as blood, water, and bio tissues [23–25]. As such, due to its potential benefits, 1–3 piezocomposites have been widely employed for the industrial [26–28] and the biomedical applications [29–31].

For decades, there have been some engineering efforts to analyze the characteristics of 1–3 piezoelectric composite through numerical simulations. For example, Hayward and Hossack examined geometric influences, such as pillar shape, pillar orientation, and pillar slope, on the dynamic and electromechanical properties in the 1–3 piezoelectric composite design, through finite element analysis (FEA) [32,33]. Hayward and Gachagan demonstrated the numerical analysis of an air-coupled 1–3 composite transducer in respect of the influence of air propagation [34]. Kim and Roh proposed a homogenizing method of 1–3 piezo composites and verified the feasibility through the FEA [35]. Kim et al. simulated mechanical stress in the interfacial area of a flexible 1–3 composite transducer [36]. Another Kim et al. demonstrated the benefits of 1–3 composite transducer with the wide frequency bandwidth, capturing pulse-like signals in an enhanced accuracy [27]. However, in past research, there has been a lack of investigations on the extensive parametric study through structure-acoustic coupled numerical analysis and the corresponding influence on the actual acoustic pressure output in interstitial FUS transducer. Therefore, given the recent increase of attention to the interstitial FUS transducers, the systematic methodology to predict the performance of such miniaturized transducers under coupled physical conditions is very substantial and meaningful to reduce engineering cost before fabricating the actual device.

The goal of this study is to design a miniaturized (<2 mm in the aperture size) FUS transducer with a 1–3 piezoelectric composite (Figure 1) and to predict the performance of the new design by using FEA. In this study, we hypothesized that the 1–3 piezoelectric material is beneficial for the efficient delivery of ultrasound waves along the thickness direction owing to the decoupling of the lateral vibration mode. The research scope of

this study is to design a miniaturized, interstitial, 1–3 piezo composite FUS transducer and to validate the feasibility through computer simulation. This article is organized as follows. In the method section, we introduce the analytical and numerical models to predict the acoustic pressure output over the acoustic field. The design method for the confocal FUS transducer is also demonstrated. The result section will provide the influence of the extensive parametric variation on the transducer performance. The simulation results will suggest the optimal design of a single 1–3 composite element and will predict the performance of the confocal transducer. Finally, we will make the relevant discussions on the simulation results, followed by the conclusion of the research. The study provides a promising, novel design of the interstitial FUS transducer capable of delivering a high acoustic intensity.

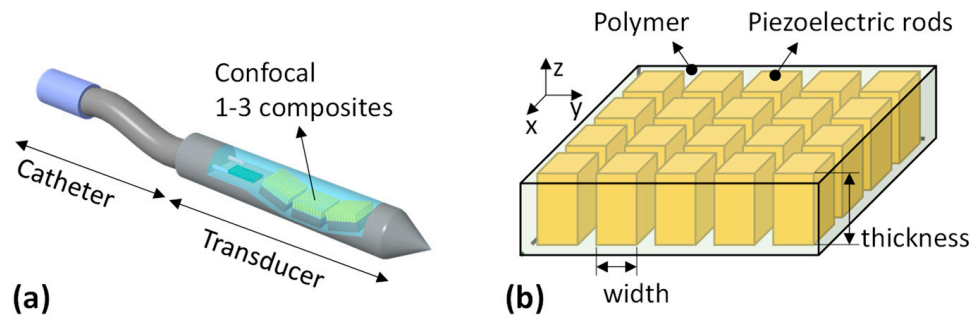


Figure 1. Schematic of the miniaturized, interstitial, focused ultrasound transducer, directed by the catheter (a), and the structure of 1–3 piezoelectric composite as an active layer (b).

2. Materials and Methods

2.1. 1–3 Piezoelectric Composite Design

Figure 1b illustrates a 1–3 composite transducer in the thickness mode. This model is symmetric of strain in the x-y direction. The transducer operates by using the E_3 field. In addition, the model satisfies the identical vertical strain and electric field requirements for polymer and piezoelectric rods.

The effective constitutive equation was derived as follows [19,37]:

$$T_{3,eff} = c_{33,eff}^E S_{3,eff} - e_{33,eff} E_{3,eff}, \tag{1}$$

$$D_{3,eff} = e_{33,eff} S_{3,eff} + \epsilon_{33,eff}^S E_{3,eff}, \tag{2}$$

where c^E , e , ϵ , T , S , D , and E are the stiffness under free electric field, piezoelectric constant, dielectric permittivity, stress, strain, electric displacement, and electric field, respectively. The superscript denotes the direction of each parameter. c^E , e , and ϵ of a 1–3 composite having the volume fractions V and \bar{V} in the active and the passive materials, were derived as follows [19,37]:

$$c_{33,eff}^E = V \left[c_{3,eff}^{c,E} - \frac{2\bar{V} \left[(c_{13}^{c,E})^2 - (c_{12}^P)^2 \right]}{V(c_{11}^P + c_{12}^P) + \bar{V}(c_{11}^{c,E} + c_{12}^{c,E})} \right] + \bar{V} c_{11}^P, \tag{3}$$

$$e_{33,eff} = V \left[e_{33}^c - \frac{2\bar{V} e_{31}^c (c_{13}^{c,E} - c_{12}^P)}{V(c_{11}^P + c_{12}^P) + \bar{V}(c_{11}^{c,E} + c_{12}^{c,E})} \right], \tag{4}$$

$$\epsilon_{33,eff}^S = V \left[\epsilon_{33}^{c,S} - \frac{2\bar{V} (e_{31}^c)^2}{V(c_{11}^P + c_{12}^P) + \bar{V}(c_{11}^{c,E} + c_{12}^{c,E})} \right] + \bar{V} \epsilon_{11}^P, \tag{5}$$

The resonance frequency (f_r) of composite transducers is determined by the relation

$$k_{t,\text{eff}} = \sqrt{\frac{\pi}{2} \frac{f_r}{f_a} \tan\left(\frac{\pi}{2} \frac{f_a - f_r}{f_a}\right)}, \quad (6)$$

$$f_a = \frac{v_{L,\text{eff}}}{2h}, \quad (7)$$

where f_r and f_a are the resonance and the anti-resonance frequencies, respectively, $k_{t,\text{eff}}$ is the effective electromechanical coupling, ρ_{eff} is the effective density, and $v_{L,\text{eff}}$ is the speed of sound in the composite.

Figure 2 shows the simulated properties of the 1–3 composite composed of PZT-4 and epoxy material. We chose PZT-4 as the active material as PZT-4 is mechanically robust while having a sufficiently high piezoelectric coefficient [38]. Its effective stiffness becomes lower than that of the single-phase material when a polymer (i.e., epoxy) with a relatively low elastic modulus is added to it (Figure 2a). The addition of the passive layer made the piezoelectric constant and the dielectric permittivity low, as shown in Figure 2b,c. By contrast, the effective coupling coefficient exhibits the maximum value in the 1–3 composite phase (Figure 2d). For example, the maximum effective coupling coefficient is approximately 0.46 at 64% of the PZT-4 volume fraction, whereas the coupling coefficient in the single-phase material is 0.38. The operation (or the resonance) frequency of the transducer is determined by the thickness of the transducer (Equations (6) and (7)). Figure 3 shows the predicted resonance frequency of the PZT-4/epoxy 1–3 composite transducer at various thicknesses of the transducer. Table 1 lists the material properties used for the analytical and numerical simulations.

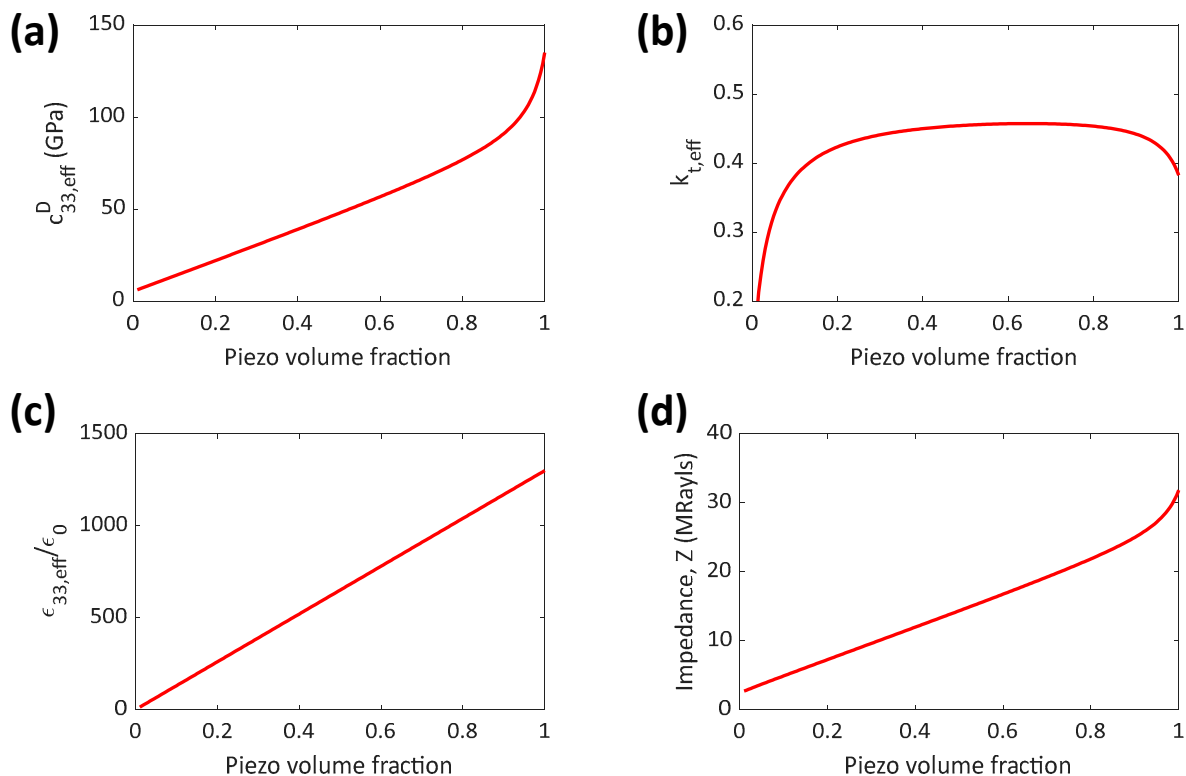


Figure 2. Effective material properties of the PZT-4/epoxy 1–3 composite; (a) mechanical stiffness, (b) electromechanical coupling, (c) dielectric permittivity, and (d) acoustic impedance.

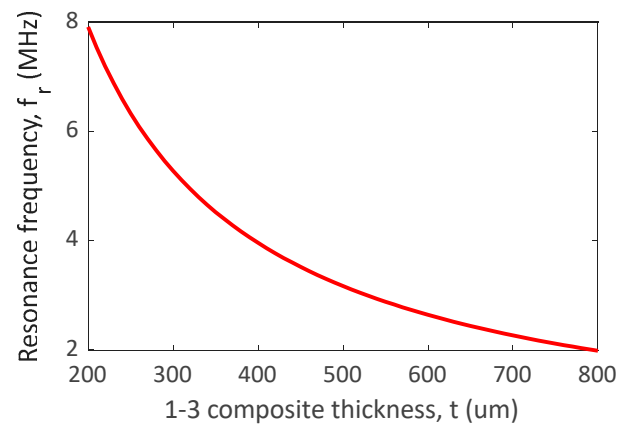


Figure 3. Prediction of the resonance frequency in the thickness vibration mode of the 1–3 piezoelectric composite transducer.

Table 1. Material properties in the numerical simulation [14,29,37].

Material	Properties	Value	
PZT-4	Density	ρ (kg/m ³)	7500
	Stiffness under free electric field	c_{11}^E ($\times 10^9$ Pa)	139.0
		c_{33}^E ($\times 10^9$ Pa)	115.4
		c_{31}^E ($\times 10^9$ Pa)	74.3
		c_{15}^E ($\times 10^9$ Pa)	25.6
	Piezoelectric coefficient	e_{31} (C/m ²)	−5.2
		e_{33} (C/m ²)	15.1
	Dielectric permittivity	$\epsilon_{11}^S/\epsilon_0$	762
		$\epsilon_{33}^S/\epsilon_0$	663
	Epoxy	Density	ρ (kg/m ³)
Stiffness		c_{31}^p ($\times 10^9$ Pa)	5.3
		c_{33}^p ($\times 10^9$ Pa)	3.1

2.2. Finite Element Analysis for Transducer Design

Figure 4 shows the procedure of the numerical simulation for the design optimization of the 1–3 piezoelectric composite transducer. First, the piezoelectric volume fraction exhibiting the maximum coupling coefficient was determined. Next, the thickness of the 1–3 composite was determined to obtain the target operation frequency at the piezoelectric volume fraction. The thickness and the volume fraction, estimated through the analytical simulation, were used as the reference information for the numerical simulation (i.e., FEA).

Figure 5a shows the finite element model and the boundary conditions. For the simulation, we used the ANSYS Workbench (v. 19.2, Canonsburg, PA, USA), a commercially available software. The 1–3 composite transducer had a piezoelectric volume fraction of 64% so that it could exhibit the maximum electromechanical coupling. It is worth noting that the analytical model cannot explain the influence of the kerf width in the composite material, which must be investigated through FEA. A voltage of 100 V (AC) and ground conditions were applied at the upper and lower surfaces of the piezoelectric rods. The mechanical vibration of the 1–3 composite transducer was transferred to the acoustic model through the fluid-structure interaction condition at the outer surfaces of the transducer. The acoustic media was set as water. The lower surface of the transducer was regarded as having air backing after applying the impedance condition of 500 Rayls [11,31]. For computation efficiency, a quarter model was utilized for the simulation.

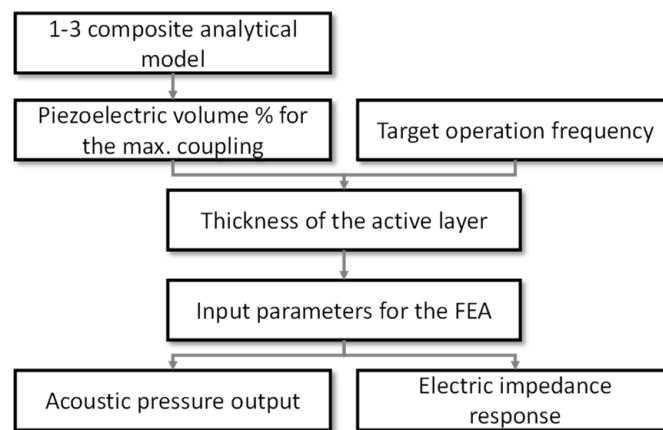


Figure 4. Design procedure of the miniaturized, 1–3 piezoelectric composite, focused ultrasound transducer.

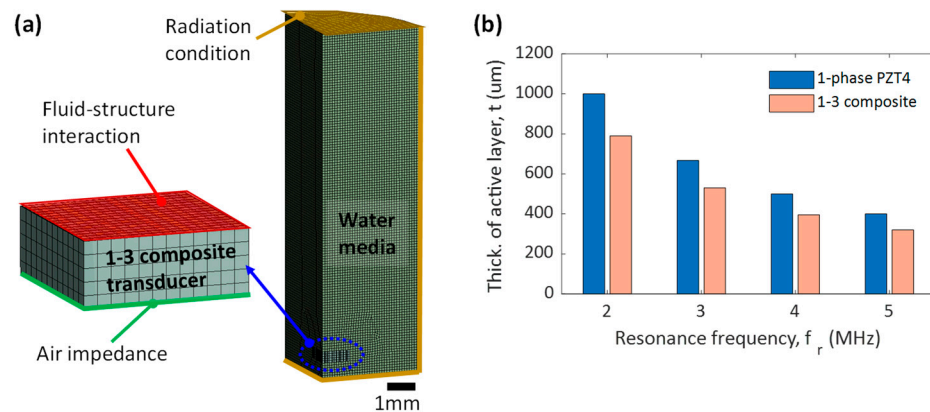


Figure 5. Boundary conditions of the numerical analysis (a) and effective thicknesses deciding the resonance frequency (b) for the prediction of the acoustic pressure output in the 1–3 composite transducer.

The pressure and the acoustic intensity outputs, produced by the single-phase and the 1–3 composite transducers, were computed through FEA and were compared with each other at the same frequency conditions for fair comparison (Figure 5b). Once the frequency effect was confirmed, the influence of the lateral size of piezoelectric rods was examined. It is noticeable that the analytical solution was estimated by the overall volumetric ratio of the piezoelectric material in the composite, ignoring the influence of the lateral vibration of the active elements.

2.3. Design of Arrayed FUS Transducer

For the side-viewing FUS device, the axial dimensions are relatively free from the dimensional restriction compared with the forward-viewing device [12,39]. Therefore, we employed the linearly aligned, confocal, miniaturized, side-viewing, FUS transducer that was composed of the 1–3 piezoelectric composite material (Figure 1a). Specifically, each transducer was aligned along the same focal distance. The confocal design was expected to be able to potentiate the resulting acoustic pressure output by concentrating the acoustic energy at the focused point. The kerf width for the final design was chosen as approximately 15 μm, corresponding to the thickness of the commercially available dicing saw. Changes in the acoustic pressure and the acoustic intensity were observed after increasing the number of participating transducer elements. The numerical simulation used the boundary conditions described in Section 2.2.

3. Results

3.1. Simulation Results for Acoustic Pressure

Figure 6 shows the acoustic pressure fields at some chosen frequencies for the single-phase and the 1–3 composite transducers. In every frequency case, the 1–3 composite transducers exhibit much higher acoustic pressure outputs compared with the single-phase transducers, as shown in Figure 7. The percentile difference in the acoustic pressure output reduced as the operating frequency increased (Figure 7). However, the acoustic pressure output in the 1–3 composite transducer was still much larger than that of the single-phase device. For example, the acoustic pressure output in the 1–3 composite was approximately 160% greater than that of the single-phase one under the 5 MHz operation condition.

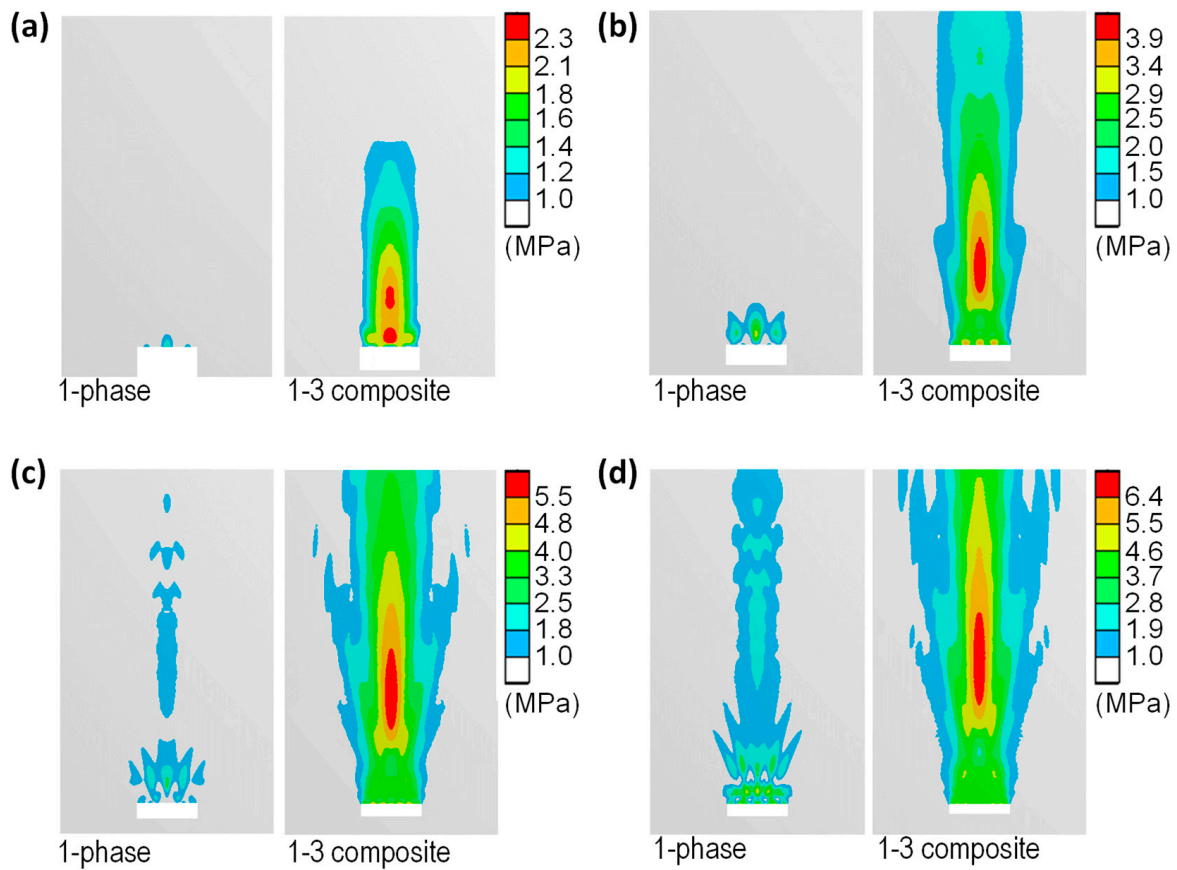


Figure 6. Comparison of the acoustic pressure fields produced by the 1-phase and the 1–3 piezoelectric composite transducers under the operation frequencies of (a) 2 MHz, (b) 3 MHz, (c) 4 MHz, and (d) 5 MHz.

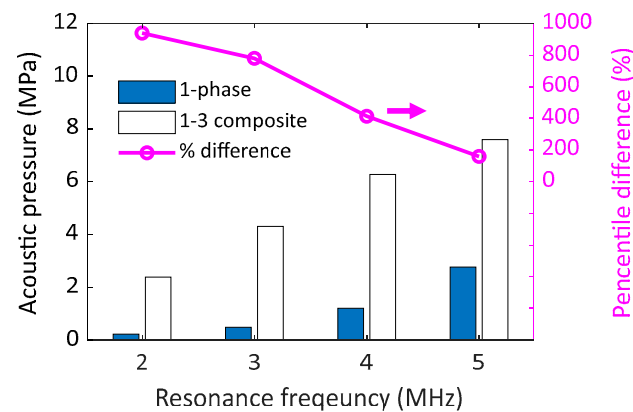


Figure 7. Comparison of acoustic pressure outputs in the single-phase and the 1–3 composite transducers at selected frequency conditions.

Figure 8 shows the variations of the acoustic pressure outputs of the 1–3 composite transducer with the width of the piezoelectric rods. The dimension ratio between the length and thickness of the piezoelectric rod had a significant effect on the acoustic pressure output. For example, the pressure level at the focal point was potentiated by decreasing the lateral dimension of each piezoelectric rod (i.e., lower dimension ratio). Table 2 lists the dimension ratios of the piezoelectric rod and the corresponding acoustic pressure outputs.

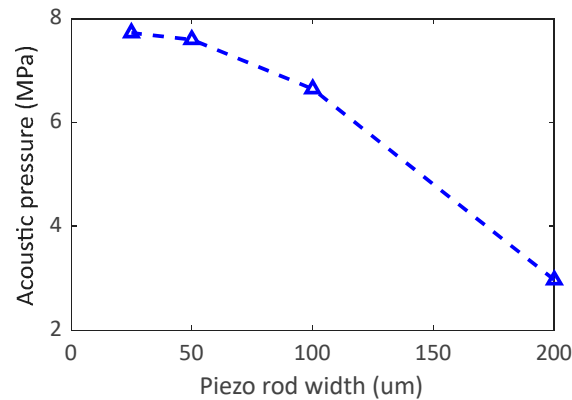


Figure 8. Acoustic pressure output at the focal point with respect to the width of the piezoelectric rods in the 1–3 composite transducer.

Table 2. Acoustic pressure output at 5 MHz with respect to the width-to-thickness ratio of the piezoelectric rod in the 1–3 composite transducer.

Width of Piezoelectric Rods (μm)	Dimension Ratio (Width-to-Thick)	Max. Pressure (MPa)	Array Dimension of the Piezoelectric Rods
200 μm	0.625	2.97	8 by 8
100 μm	0.313	6.65	16 by 16
50 μm	0.156	7.60	32 by 32
25 μm	0.078	7.73	64 by 64

3.2. Simulation Results for Electric Impedance

The mechanism affecting the performance of the 1–3 piezoelectric composite was examined through the electric impedance responses. Figure 9 presents a comparison of the electric impedances of the single-phase and the 1–3 composite transducers at each frequency condition. Electric impedance in the single-phase transducer did not show a clear resonance peak at the designed thickness of the piezoelectric material. Nonetheless, at higher frequency conditions (e.g., 5 MHz in Figure 9d), the resonance peak became more dominant, approaching the designed frequency range. Therefore, the 5 MHz, single-phase transducer could produce a relatively high acoustic pressure output compared with the lower frequency cases.

By contrast, electric impedance in the 1–3 composite transducer exhibited the predominant resonance peak at the designed frequency range. The frequency bandwidth was also relatively broad for the 1–3 composite design. Moreover, the secondary resonance frequencies were far from the main resonance band. Figure 10 shows the variation in the electric impedance curve with respect to changes in the dimension ratio of the piezoelectric rod in the 1–3 piezoelectric composite. At a high dimensional ratio (e.g., 200/320 μm, width/thickness), the frequency peak at resonance seems to be affected by the other vibration mode, showing a kind of discontinuity around the resonance and the anti-resonance frequencies. Nonetheless, in all the width cases except the 200 μm case, the impedance level and the resonance frequency were all very similar, with a difference of approximately 2%.

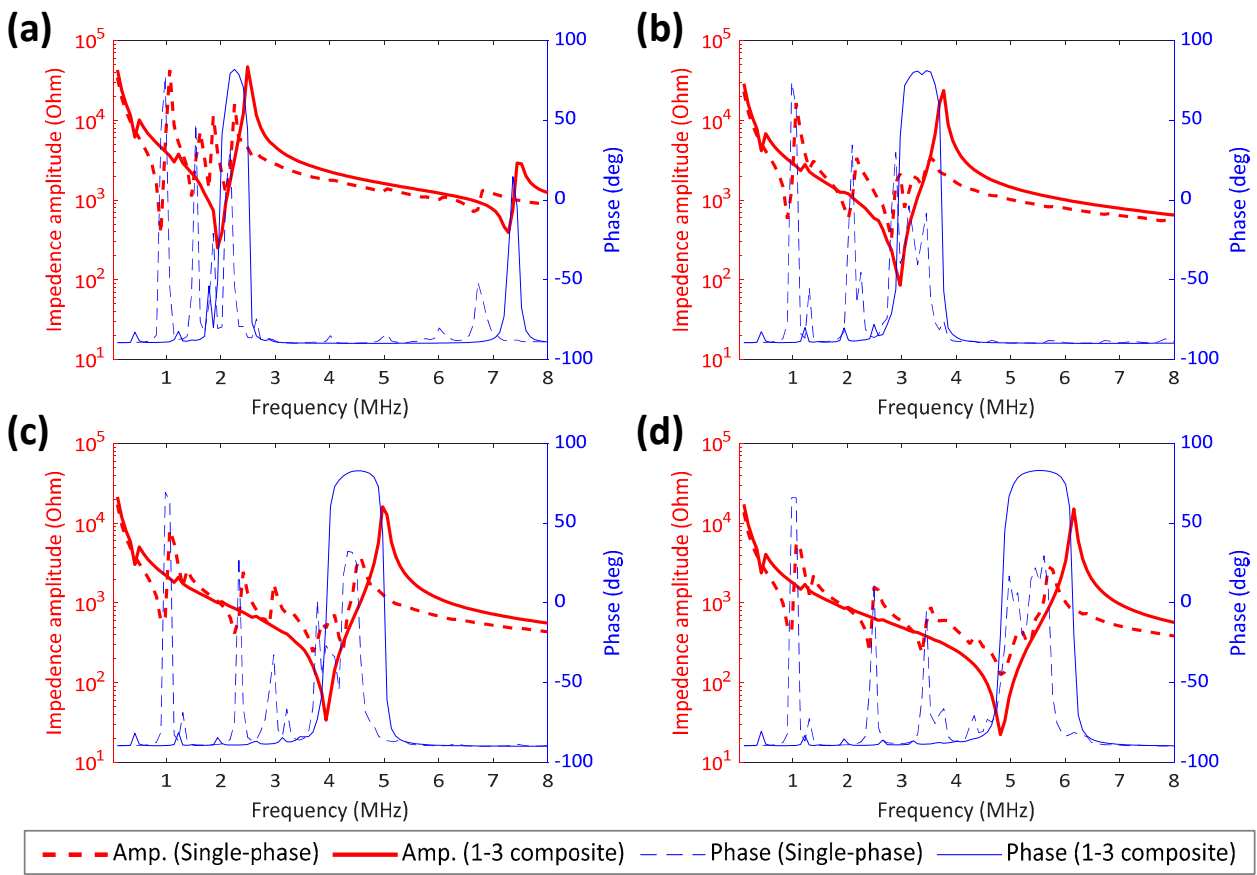


Figure 9. Electric impedance responses of the single- and the 1–3 composite transducers designed for (a) 2 MHz, (b) 3 MHz, (c) 4 MHz, and (d) 5 MHz.

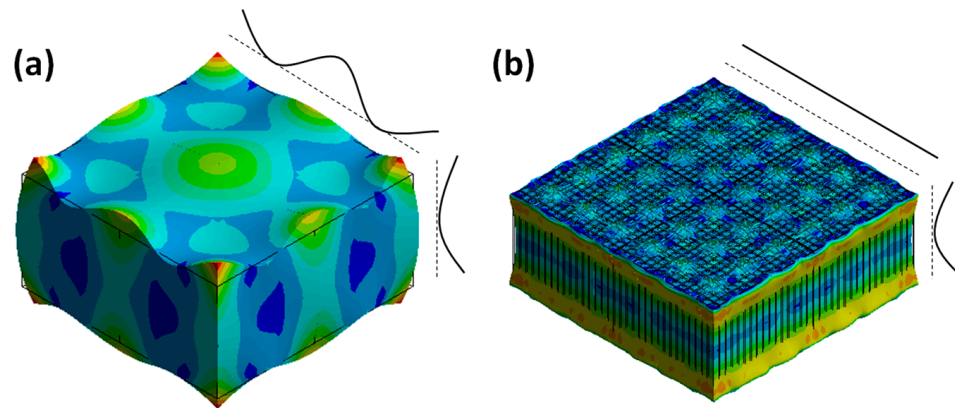


Figure 10. Vibration mode shapes at the operation frequency (2 MHz) of (a) the single-phase and (b) the 1–3 composite transducers, where the solid and the dashed lines denote the mode shapes and the neutral line.

3.3. Simulation of Confocal, Linear Array, Transducer

The mechanism affecting the performance of the 1–3 piezoelectric composite was examined through the electric impedance responses. The simulation was conducted with free boundary conditions to observe the vibration mode shape related to the transducer structure only. The unit and zero voltages are applied at the top and the bottom surfaces, respectively. Figure 9 compares the electric impedances of the single-phase and the 1–3 composite transducers at each frequency condition. Electric impedance in the single-phase transducer did not show the clear resonance peak at the designed thickness of the

piezoelectric material. For example, Figure 10 demonstrates the vibration mode shapes in the single and the 1–3 composite transducers. The 1–3 composite transducer predominantly deformed along the thickness direction while the lateral vibration was well suppressed. In contrast, vibration pattern in the single-phase transducer was highly affected by the higher modes of the lateral vibration. Nonetheless, at higher frequency conditions (e.g., 5 MHz in Figure 9d), the resonance peak became more dominant, approaching the designed frequency range. Therefore, the 5-MHz, single-phase transducer could produce a relatively high acoustic pressure output compared to the lower frequency cases.

In contrast, electric impedance in the 1–3 composite transducer exhibited the predominant resonance peak at the designed frequency range. The frequency bandwidth was also relatively broad with the 1–3 composite design. Moreover, the secondary resonance frequencies were far apart from the main resonance band. Figure 11 shows the variation of the electric impedance curve with respect to the change in the dimension ratio of the piezoelectric rod in the 1–3 piezoelectric composite. In a high dimensional ratio (e.g., $>200/320 \mu\text{m}$, width/thickness), the frequency peak at the resonance seems like being affected by the other vibration mode, showing a kind of discontinuity around the resonance and the anti-resonance frequencies. Nonetheless, in the width cases below $200 \mu\text{m}$, the impedance level and the resonance frequency were all very similar with a difference of about 2%.

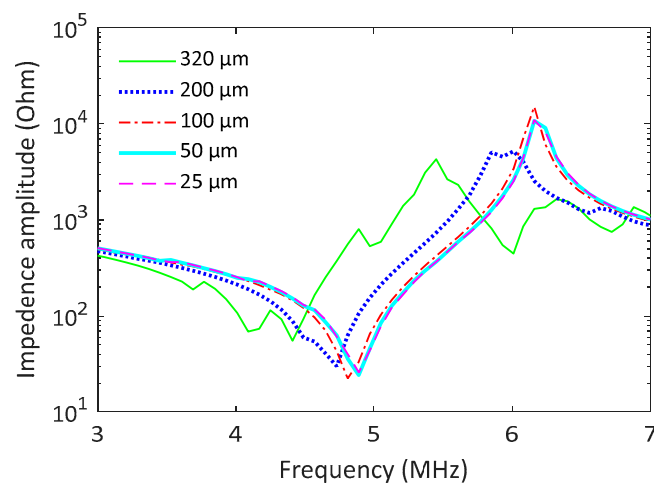


Figure 11. The amplitude of electric impedance responses with respect to the width of piezoelectric rods in the 1–3 composite transducers.

3.4. Simulation of Confocal Transducer

The advantages of the 1–3 composite transducer were confirmed by comparing the performances of the 1–3 composite and the single-phase transducers. Based on the confirmed design of the 1–3 composite, a confocal transducer was designed to further intensify the pressure output. Few additional active elements were deployed along with using the identical focal point, where the focal point was given by the focal depth (i.e., 4.3 mm) estimated from the single 1–3 composite transducer.

Figure 12a shows the acoustic pressure fields achieved by the multi-element of 1–3 composite piezoelectric transducers, where the volumetric percentage is 64% and the rod width is $61.5 \mu\text{m}$ for the piezoelectric material. As shown in Figure 12a,b, the acoustic pressure and the acoustic intensity were magnified by employing more transducers and focusing the acoustic beam on the identical focal point. The electric impedance level at the resonance was also reduced by adding more active elements (Figure 12c). Table 3 summarizes the performance of the miniaturized, 3-by-1 arrayed 1–3 composite piezoelectric transducer. The maximum acoustic pressure output reached over approximately 23.6 MPa in the zero-to-peak level on applying just 100 V (AC) to the miniaturized FUS device. The acoustic intensity in the spatial-peak time-averaged level was estimated as approximately

188 W/cm² with a short duty cycle (i.e., 1%). Finally, the high acoustic area over 20 MPa was positioned within a spatial boundary of approximately 1 mm.

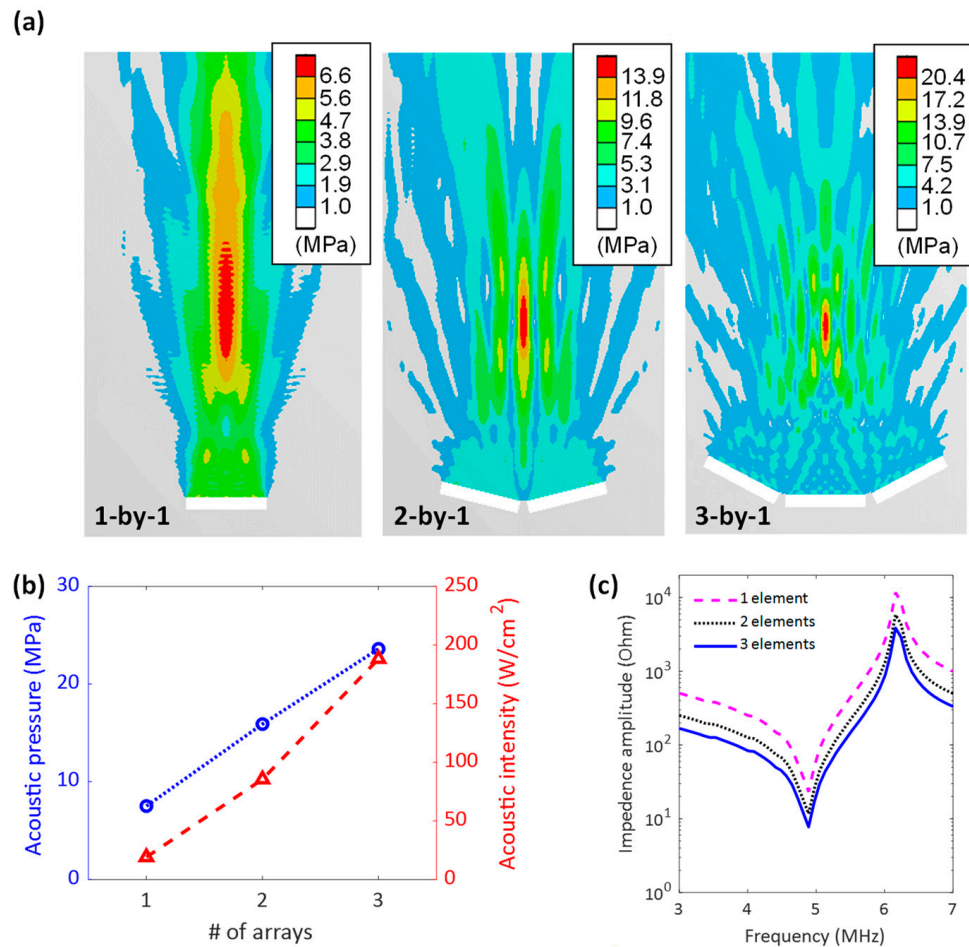


Figure 12. Simulated performance of the 1–3 composite focused ultrasound transducer; (a) the acoustic pressure field with respect to the number of the transducer elements, (b) the acoustic pressure output and the acoustic intensity with respect to the number of arrays, and (c) electric impedance responses with the varying number of active elements in the water media.

Table 3. Simulated specification of the designed focused ultrasound transducer.

Specification	Unit	Value	Specification	Unit	Value
Num. of elements	-	3 by 1	Acoustic intensity	W/cm ²	188.2
Aperture size	mm ²	2 × 2	Acoustic pressure	MPa	23.6
Operation freq.	MHz	5 MHz	Electric impedance	Ohm	7.8

4. Discussion

The numerical simulation results revealed the performances of the single-phase and the 1–3 composite transducers. The single-phase transducer could not produce a higher acoustic pressure output than the 1–3 composite one, as shown in Figures 6 and 7. This is because the thickness of the active layer, which determines the operation frequency, approaches the lateral size of the active element in relatively low-frequency operation conditions (e.g., <5 MHz). The close resonance frequencies of the vertical and the lateral vibrations cause coupling of the vibration modes. Figure 9 shows the vibration coupling in the electric impedance response. For example, for the single-phase transducers (i.e., dashed lines), the lateral vibration modes are found in many different frequency bands, which

interfere with the thickness vibration mode. Consequently, the high impedance due to the mode coupling has an adverse effect on the generation of the acoustic pressure output from the FUS transducer. However, the influence of the vibration coupling in the miniaturized transducer design is difficult to eliminate in the typical single-phase transducer as the lateral dimension of the active layer must be relatively small in accordance with the size of the lumen where the FUS device would travel in the human body.

By contrast, the electric impedance curve in the 1–3 composite design shows a clear resonance with a relatively broad frequency band (Figure 9). The high electromechanical coupling (e.g., ~46% in the 1–3 composite and ~38% in the single-phase) and the predominant thickness vibration mode could produce a relatively high acoustic pressure output, as shown in Figure 6. The lateral dimension of the small piece of the piezoelectric rods was differentiated from the thickness size by employing the 1–3 composite design, which resulted in the de-coupling of the lateral and the thickness vibration modes. Nonetheless, the width of the single piezoelectric rod in the 1–3 composite could still affect the performance of the transducer in the case where the width was not small enough compared to the thickness. Specifically, even though there was no significant change in the electric impedance with respect to the lateral dimension (Figure 11), the acoustic pressure output was affected by the lateral size of the single piezoelectric rods in the 1–3 composite (Figure 8). For a relatively large lateral dimension, the dimensional ratio became small, causing interference of the lateral vibration mode and the corresponding low acoustic pressure output along the thickness direction. Therefore, the dimension ratio of the piezoelectric rod in the 1–3 composite needs to be small enough ($< \sim 1:6$) to isolate the mode coupling effect. In other words, according to the simulation results, it was suggested that the width of the piezoelectric rod should be approximately six times smaller than the thickness. However, a too-small size of the piezoelectric rods may compromise the feasibility of fabrication.

We, in this study, determined the geometric parameters of a single 1–3 piezo composite based on the simple procedure described in Figure 4. The approach assumed that the transducer with design parameters chosen by the maximum coupling value would produce the almost maximum acoustic pressure output. However, as shown in Figure 2b, the electromechanical coupling slightly changes in the span of from about 0.25 to 0.94 of the piezoelectric volume fractions. Therefore, we examined if the criteria to select the maximum coupling region would be reliable. For example, -5% reduction in the coupling value compared to the maximum makes two opposite scenarios; the first condition exhibits low acoustic impedance (i.e., reduction in the acoustic mismatch) (Figure 13a), yet the second one occupies a dense piezoelectric volume while compromising the acoustic impedance (Figure 13c). The thickness of the transducer was, in each simulation model, adjusted to correspond to the new speed of sound, caused by the change of electromechanical coupling. Figure 13a,c demonstrated the trade-off between the acoustic impedance and the piezo volume fraction. Therefore, the selection of the maximum electromechanical coupling can be a decent criterion for designing the FUS transducer design. Once the performance of a single 1–3 composite element is confirmed, the additional design effort can be made in terms of the matching, the backing, and the confocal design.

For example, in Figure 12, the multi-element, confocal, 1–3 composite transducer was capable of delivering an acoustic pressure of approximately 23.6 MPa with a 100 V (AC) application. The corresponding acoustic intensity was over 188 W/cm² in a short duty cycle (i.e., 1%). The spatial resolution of the maximum pressure region was also improved by employing the arrayed FUS design and concentrating the acoustic energy at a spot. Therefore, the new therapeutic FUS device designed in this study can be used in new clinical applications, such as in precise, interstitial (or intravascular) histotripsy. In the future, we shall investigate miniaturized, confocal, 1–3 piezoelectric composite transducers for application to tissue ablation in an interstitial manner using high acoustic intensity with precise spatial resolution under a low electric input power.

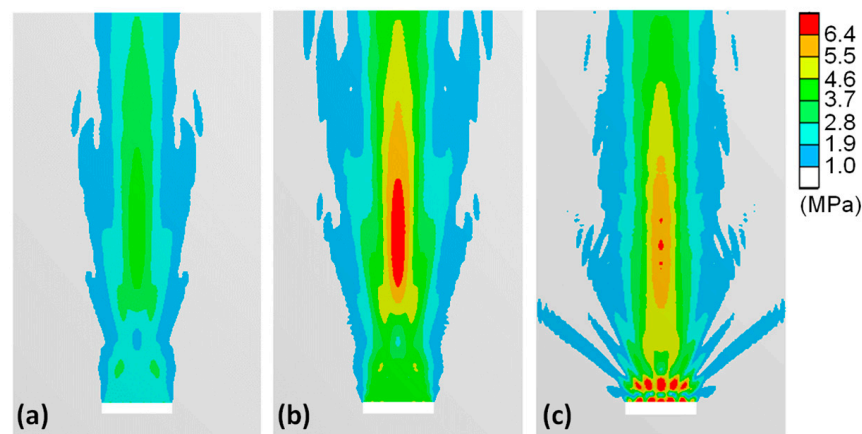


Figure 13. Comparison of acoustic pressure fields in the variation of electromechanical coupling; (a) lower (−5%) electromechanical coupling (43.5%), low acoustic impedance (8.5 MRayls), (b) maximum electromechanical coupling (45.8%), and (c) lower (−5%) electromechanical coupling, denser piezoelectric volume (93%).

5. Conclusions

In this study, we investigated a miniaturized (<2 mm in diameter), 1–3 composite FUS transducer with the aid of coupled numerical analysis. This study suggested a systematic design process and implemented extensive parametric studies for the design of the new miniaturized FUS transducer. The 1–3 composite transducer does not have the technical restrictions of the conventional single-phase transducer such as the mode coupling issue. Therefore, the 1–3 composite transducer could produce a high acoustic pressure of approximately 7.6 MPa that is much greater (>160%) than that of the single-phase one. Furthermore, the parametric study demonstrated that the thin kerf width in the 1–3 composite design would be desirable for obtaining a high acoustic pressure output. Based on the parametric studies, a 3-by-1 FUS transducer was designed. The new device was predicted to deliver an unprecedented level of the acoustic pressure output (>20 MPa) and acoustic intensity ($\sim 188 \text{ W/cm}^2$) in a narrow spot (<1 mm). Therefore, the new transducer design can be utilized for precise tissue ablation inside the human body. In future work, we will implement the verification of the actual performance of the device for therapeutic applications.

Author Contributions: Conceptualization, H.K. and X.J.; methodology, H.K.; simulation, H.K.; validation, H.K.; writing—original draft preparation, H.K.; review, X.J. All authors have read and agreed to the published version of the manuscript.

Funding: This work was supported in part by DOD under W81XWH-22-1-0285. This work was also supported in part by the INHA University Research Grant (INHA-68646).

Institutional Review Board Statement: Not applicable.

Informed Consent Statement: Not applicable.

Data Availability Statement: Not applicable.

Acknowledgments: The author would like to acknowledge the INSTAR program at Inha University for granting an ANSYS software license.

Conflicts of Interest: The author declares no conflict of interest.

References

1. Ter Haar, G. HIFU Tissue Ablation: Concept and Devices. In *Therapeutic Ultrasound*; Escoffre, J.M., Bouakaz, A., Eds.; Springer: Plan-les-Ouates, Switzerland, 2016; Volume 880, pp. 3–20.
2. Mason, T.J. Therapeutic ultrasound an overview. *Ultrason. Sonochem.* **2011**, *18*, 847–852. [[CrossRef](#)] [[PubMed](#)]
3. Ter Haar, G.; Coussios, C. High intensity focused ultrasound: Physical principles and devices. *Int. J. Hyperth.* **2007**, *23*, 89–104. [[CrossRef](#)] [[PubMed](#)]

4. Izadifar, Z.; Izadifar, Z.; Chapman, D.; Babyn, P. An introduction to high intensity focused ultrasound: Systematic review on principles, devices, and clinical applications. *J. Clin. Med.* **2020**, *9*, 460. [[CrossRef](#)]
5. Al-Bataineh, O.; Jenne, J.; Huber, P. Clinical and future applications of high intensity focused ultrasound in cancer. *Cancer Treat. Rev.* **2012**, *38*, 346–353. [[CrossRef](#)] [[PubMed](#)]
6. Zhang, X.; Macoskey, J.J.; Ives, K.; Owens, G.E.; Gurm, H.S.; Shi, J.; Pizzuto, M.; Cain, C.A.; Xu, Z. Non-invasive thrombolysis using microtripsy in a porcine deep vein thrombosis model. *Ultrasound Med. Biol.* **2017**, *43*, 1378–1390. [[CrossRef](#)] [[PubMed](#)]
7. Klingler, H.C.; Susani, M.; Seip, R.; Mauermann, J.; Sanghvi, N.; Marberger, M.J. A novel approach to energy ablative therapy of small renal tumours: Laparoscopic high-intensity focused ultrasound. *Eur. Urol.* **2008**, *53*, 810–818. [[CrossRef](#)] [[PubMed](#)]
8. Li, J.J.; Xu, G.L.; Gu, M.F.; Luo, G.Y.; Rong, Z.; Wu, P.H.; Xia, J.C. Complications of high intensity focused ultrasound in patients with recurrent and metastatic abdominal tumors. *World. J. Gastroenterol.* **2007**, *13*, 2747. [[CrossRef](#)]
9. Merckel, L.G.; Knuttel, F.M.; Deckers, R.; van Dalen, T.; Schubert, G.; Peters, N.H.; Weits, T.; van Diest, P.J.; Mali, W.P.; Vaessen, P.H.; et al. First clinical experience with a dedicated MRI-guided high-intensity focused ultrasound system for breast cancer ablation. *Eur. Radiol.* **2016**, *26*, 4037–4046. [[CrossRef](#)]
10. Azhari, H. Feasibility study of ultrasonic computed tomography-guided high-intensity focused ultrasound. *Ultrasound. Med. Biol.* **2012**, *38*, 619–625. [[CrossRef](#)]
11. Kim, H.; Kim, J.; Wu, H.; Zhang, B.; Dayton, P.A.; Jiang, X. A multi-pillar piezoelectric stack transducer for nanodroplet mediated intravascular sonothrombolysis. *Ultrasonics* **2021**, *116*, 106520. [[CrossRef](#)]
12. Lafon, C.; Melodelima, D.; Salomir, R.; Chapelon, J.Y. Interstitial devices for minimally invasive thermal ablation by high-intensity ultrasound. *Int. J. Hyperth.* **2007**, *23*, 153–163. [[CrossRef](#)] [[PubMed](#)]
13. Zhang, B.; Wu, H.; Goel, L.; Kim, H.; Peng, C.; Kim, J.; Dayton, P.A.; Gao, Y.; Jiang, X. Magneto-sonothrombolysis with combination of magnetic microbubbles and nanodroplets. *Ultrasonics* **2021**, *116*, 106487. [[CrossRef](#)]
14. Kim, H.; Wu, H.; Cho, N.; Zhong, P.; Mahmood, K.; Lyerly, H.K.; Jiang, X. Miniaturized intracavitary forward-looking ultrasound transducer for tissue ablation. *IEEE Trans. Biomed. Eng.* **2019**, *67*, 2084–2093. [[CrossRef](#)]
15. Canney, M.S.; Chavrier, F.; Tsygar, S.; Chapelon, J.Y.; Lafon, C.; Carpentier, A. A multi-element interstitial ultrasound applicator for the thermal therapy of brain tumors. *J. Acoust. Soc. Am.* **2013**, *134*, 1647–1655. [[CrossRef](#)]
16. Kim, H.; Wu, H.; Chen, M.; Dai, X.; Zhou, R.; Jiang, X. Intravascular sono-ablation for in-stent restenosis relief: Transducer development and the in-vitro demonstration. *IEEE Trans. Biomed. Eng.* **2023**; submitted.
17. Vazquez Carazo, A. Piezoelectric transformers: An historical review. *Actuators* **2016**, *5*, 12. [[CrossRef](#)]
18. Refahati, N.; Jearsiripongkul, T.; Thongchom, C.; Saffari, P.R.; Saffari, P.R.; Keawsawasvong, S. Sound transmission loss of double-walled sandwich cross-ply layered magneto-electro-elastic plates under thermal environment. *Sci. Rep.* **2022**, *12*, 16621. [[CrossRef](#)] [[PubMed](#)]
19. Kim, H.; Yuan, F.G. Adaptive signal decomposition and dispersion removal based on the matching pursuit algorithm using dispersion-based dictionary for enhancing damage imaging. *Ultrasonics* **2020**, *103*, 106087. [[CrossRef](#)] [[PubMed](#)]
20. Yamashita, Y.; Karaki, T.; Lee, H.Y.; Wan, H.; Kim, H.P.; Jiang, X. A Review of Lead Perovskite Piezoelectric Single Crystals and Their Medical Transducers Application. *IEEE Trans. Ultrason. Ferroelectr. Freq. Control* **2022**, *69*, 3048–3056. [[CrossRef](#)]
21. Zhang, S.; Li, F.; Yu, F.; Jiang, X.; Lee, H.Y.; Luo, J.; Shrout, T.R. Recent developments in piezoelectric crystals. *J. Korean Ceram. Soc.* **2018**, *55*, 419–439. [[CrossRef](#)]
22. Lerch, R. Simulation of piezoelectric devices by two-and three-dimensional finite elements. *IEEE Trans. Ultrason. Ferroelectr. Freq. Control* **1990**, *37*, 233–247. [[CrossRef](#)]
23. Smith, W.A.; Auld, B.A. Modeling 1–3 composite piezoelectrics: Thickness-mode oscillations. *IEEE Trans. Ultrason. Ferroelectr. Freq. Control* **1991**, *38*, 40–47. [[CrossRef](#)]
24. Sun, R.; Wang, L.; Zhang, Y.; Zhong, C. Characterization of 1–3 piezoelectric composite with a 3-tier polymer structure. *Materials* **2020**, *13*, 397. [[CrossRef](#)]
25. Zhou, W.; Zhang, T.; Ou-Yang, J.; Yang, X.; Wu, D.; Zhu, B. PIN-PMN-PT single crystal 1–3 composite-based 20 MHz ultrasound phased array. *Micromachines* **2020**, *11*, 524. [[CrossRef](#)]
26. Cheng, X.; Xu, D.; Lu, L.; Huang, S.; Jiang, M. Performance investigation of 1–3 piezoelectric ceramic–cement composite. *Mater. Chem. Phys.* **2010**, *121*, 63–69. [[CrossRef](#)]
27. Kim, H.; Kim, T.; Morrow, D.; Jiang, X. Stress measurement of a pressurized vessel using ultrasonic subsurface longitudinal wave with 1–3 composite transducers. *IEEE Trans. Ultrason. Ferroelectr. Freq. Control* **2019**, *67*, 158–166. [[CrossRef](#)]
28. Kim, J.; Li, S.; Kasoji, S.; Dayton, P.A.; Jiang, X. Phantom evaluation of stacked-type dual-frequency 1–3 composite transducers: A feasibility study on intracavitary acoustic angiography. *Ultrasonics* **2015**, *63*, 7–15. [[CrossRef](#)] [[PubMed](#)]
29. Kim, T.; Kim, J.; Jiang, X. Transit time difference flowmeter for intravenous flow rate measurement using 1–3 piezoelectric composite transducers. *IEEE Sens. J.* **2017**, *17*, 5741–5748. [[CrossRef](#)]
30. Li, S.; Tian, J.; Jiang, X. A micromachined Pb (Mg_{1/3}Nb_{2/3})O₃-PbTiO₃ single crystal composite circular array for intravascular ultrasound imaging. *J. Eng. Sci. Med. Diagn. Ther.* **2019**, *2*, 021001. [[CrossRef](#)]
31. Ma, J.; Guo, S.; Wu, D.; Geng, X.; Jiang, X. Design, fabrication, and characterization of a single-aperture 1.5-MHz/3-MHz dual-frequency HIFU transducer. *IEEE Trans. Ultrason. Ferroelectr. Freq. Control* **2013**, *60*, 1519–1529. [[CrossRef](#)]
32. Hossack, J.A.; Hayward, G. Finite-element analysis of 1–3 composite transducers. *IEEE Trans. Ultrason. Ferroelectr. Freq. Control* **1991**, *38*, 618–629. [[CrossRef](#)]

33. Hayward, G.; Bennett, J. Assessing the influence of pillar aspect ratio on the behavior of 1–3 connectivity composite transducers. *IEEE Trans. Ultrason. Ferroelectr. Freq. Control* **1996**, *43*, 98–108. [[CrossRef](#)]
34. Hayward, G.; Gachagan, A. An evaluation of 1–3 connectivity composite transducers for air-coupled ultrasonic applications. *J. Acoust. Soc. Am.* **1996**, *99*, 2148–2157. [[CrossRef](#)]
35. Kim, J.; Roh, Y. Homogenization of PMN-PT/epoxy 1–3 piezocomposites by resonator measurements and finite element analysis. *Sens. Actuator. A Phys.* **2014**, *206*, 97–106. [[CrossRef](#)]
36. Kim, T.; Cui, Z.; Chang, W.Y.; Kim, H.; Zhu, Y.; Jiang, X. Flexible 1–3 composite ultrasound transducers with silver-nanowire-based stretchable electrodes. *IEEE Trans. Ind. Electron.* **2019**, *67*, 6955–6962. [[CrossRef](#)]
37. Kim, H. Design, Prototyping, and Validation of Noninvasive Sensors for Nuclear Power Plant Applications. Ph.D. Thesis, North Carolina State University, Raleigh, NC, USA, May 2020.
38. Fan, J.; Stoll, W.A.; Lynch, C.S. Nonlinear constitutive behavior of soft and hard PZT: Experiments and modeling. *Acta Mater.* **1999**, *47*, 4415–4425. [[CrossRef](#)]
39. Owens, C.A. Ultrasound-enhanced thrombolysis: EKOS EndoWave infusion catheter system. *Semin. Interv. Radiol.* **2008**, *25*, 37–41. [[CrossRef](#)]

Disclaimer/Publisher’s Note: The statements, opinions and data contained in all publications are solely those of the individual author(s) and contributor(s) and not of MDPI and/or the editor(s). MDPI and/or the editor(s) disclaim responsibility for any injury to people or property resulting from any ideas, methods, instructions or products referred to in the content.